Optically Detected Magnetic Resonance Study of Electron/Hole Traps on CdSe Quantum Dot Surfaces

E. Lifshitz,* I. Dag, and I. D. Litvitn

Department of Chemistry and Solid State Institute, Technion, Haifa, 32000, Israel

G. Hodes

Department of Materials and Interfaces, The Weizmann Institute of Science, Rehovot, 76100, Israel

Received: April 15, 1998; In Final Form: July 15, 1998

Thin films of CdSe nanoparticles were chemically deposited on a glass substrate. The PL spectra of these films are dominated by a red-IR emission band, associated with the recombination of shallow trapped electrons and deep trapped holes. The optically detected magnetic resonance (ODMR) measurements revealed that the trapping sites have low symmetry, thus suggesting their existence at the surface of the nanoparticles. Moreover, the theoretical simulation suggests a distribution of e−h pair distances, leading to an ensemble of exchange interaction values. The trapping sites are distributed around the circumference of the nanoparticles, and the e−h spatial separation is therefore limited by the size of the nanoparticles. The *g* values of the trapped carriers are substantially different from those of the band edge, further supporting the idea of trapped carrier localization at imperfection sites.

Introduction

In the past decade there has been increasing interest in the scientific and technological aspects of dispersed nanometer-sized semiconductors (nanoparticles), prepared by chemical reactions. These nanoparticles exhibit unique characteristics, associated with the quantum size effect and with the existence of a relatively large percentage of atoms at the surface. In recent years, semiconductor nanoparticles of the II−VI, III−V, II−V, and IV−VI compounds have been prepared in colloidal solutions[1−3] or embedded in glass,[4] polymers,[5] or zeolite cages.[6] In these media, the nanoparticles can be prepared with a high degree of reproducibility, controlled diameters of <10 nm, relatively narrow size distribution (<5−15%), and uniform shape.[1] The experimental and theoretical aspects of the quantum size effect and electronic properties of individual nanoparticles have been treated extensively in several major publications.[7,8]

The extensive study of dispersed nanoparticles has stimulated preliminary work in the engineering and investigation of deposited nanoparticles in the form of thin films. The latter show an advantage when deposited on a metal substrate, by providing a direct method of integrating the nanoparticles into optoelectronic and electrochemical architectures. The chemical solution deposition (CD) method has been used for many decades to deposit films of chalcogenide semiconductors. For example, CD films of PbS and PbSe nanoparticles were utilized as photoconduction detectors.[9] More recently, CD has become the standard method to deposit CdS buffer layers in thin-film photovoltaic cells,[10,11] which has led to increased interest in the CD technique in general. Hodes et al.[12−14] showed that CdSe and PbSe films, deposited by CD, were comprised of aggregates of nanoparticles (typically 5 nm in size) that exhibit strong quantum confinement effects.

Either in the dispersed or in the deposited film configuration, the electronic and optical properties of the nanoparticles will be governed by the properties of the surfaces and interfaces. The large fraction of surface atoms leads to the existence of a large number of dangling bonds, stoichiometric or external adatoms. The latter play a key role in structural transformations,[15,16] solubility,[17] melting point of the materials,[18] localization of carriers, and light emission processes.[19,20] Recently, we showed that the photoluminescence (PL) spectrum of CD CdSe nanoparticles includes a nonexcitonic emission band associated with surface states.[21] The results have indicated that this band involves the recombination between shallow trapped electrons and deep trapped holes, with a donor−acceptor-like recombination emission. The present publication extends our preliminary observation by a thorough investigation of the recombination mechanism of the nonexcitonic emission band. This study includes the utilization of optically detected magnetic resonance (ODMR) spectroscopy of CD CdSe nanoparticle films, with mean particle diameters of 4, 6, and 20 nm.

Experimental Section

Materials Preparation. The deposition solution was prepared by mixing cadmium nitriloacatate solution (1) with a sodium selenosulfate solution (2). Solution 1 was prepared by diluting a 0.5 M $CdSO_4$ solution with water, adding a 0.7 M potassium nitrilotriacetic acid (K_3NTA) solution, and adjusting the pH with KOH solution ca. 8.5. Solution 2 was prepared by stirring 0.2 M Se with 0.5 M Na_2SO_3 at ca. 70 °C for several hours, leading to the formation of Na_2SeSO_3. After mixing, the pH was adjusted to 10.0 with KOH solution. The composition of the final solution was 80 mM $CdSO_4$, 80 mM Na_2SeSO_3, and 120−190 mM K_3NTA. The films were deposited on a glass substrate immersed in the deposition solution in a thermostatically controlled water bath, at the required temperature, ranging between 10 and 80 °C. The glass substrate was positioned almost vertically in the deposition solution to minimize the deposition of bulk material. The deposition time was typically between 10 h to several days, and the resulting film thickness

10.1021/jp981880v CCC: $15.00
Published on Web 10/22/1998

was about 100 nm. The deposited film facing downward in the solution was retained on the substrate for the measurements. The film, deposited on the upper part of the substrate, was removed with a cotton swab, moistened with dilute (ca. 2 M) HCl. Additional details associated with the chemical solution deposition method are described in refs 22 and 23.

The size of the CdSe nanoparticles, deposited in the above manner, depends mainly on the deposition temperature and the $K_3NTA:Cd^{2+}$ concentration ratio. A K_3NTA concentration of 120 mM in the final solution, and a deposition temperature of 10 °C at the final stages, led to the formation of 4 nm particles. Both 130 mM K_3NTA and a deposition temperature of 60 °C produced the 6 nm particles, while 170 mM K_3NTA and a deposition temperature of 60−80 °C produced the 20 nm particles. Clearly, the elevated temperatures led to the growth of larger crystals. An increase in the $K_3NTA:Cd^{2+}$ ratio above a certain limit (with a dependence on various other parameters) resulted in the formation of larger crystals, due to a change in the deposition mechanism, as discussed in refs 22 and 23. The crystallographic structure and size of the nanoparticles were measured by X-ray diffraction (XRD) and TEM. The XRD and TEM measurements of the CD CdSe nanoparticles films are reported in refs 22 and 23. These measurements indicate that the particles possess cubic crystallographic structure, with average diameter between 4 and 20 nm and a size distribution of about 15%. Furthermore, the diffraction measurements revealed that the nanoparticles are randomly oriented within the films.

Instruments. The optical transmittance spectra of the CdSe films on glass substrates were recorded using a Uvikon 810 UV−vis spectrophotometer with glass as a reference. The absorbance spectra shown below were not corrected for reflectance of the samples.

The PL measurements were carried out by placing the samples in a cryogenic dewar and exciting them with continuous 457.9 or 514.0 nm Ar^+ laser. The emitted light was passed through an holographic grating monochromator and detected by a photomultiplier tube. ODMR spectra were obtained by measuring the change in luminescence intensity, ΔI_{PL} (or its circular component), induced by a magnetic resonance event at the excited state. Then ΔI_{PL} was plotted versus the strength of the external magnetic field, H_0, leading to magnetic resonance-like spectra. The induced change was monitored either at a specific emission energy or through detection of the total luminescence band. ODMR spectra were recorded by immersing the sample in a cryogenic dewar (2 K) centered within a High-Q resonance cavity, coupled to a microwave (mw) source (9 GHz) and surrounded by a superconducting magnet. The ODMR signal was detected in either of the following configurations: (a) in a k_{em} direction, parallel to the external magnetic field ($k_{em}||H_0$, Faraday configuration) or (b) in a direction perpendicular to H_0 ($k_{em}\perp H_0$, Voight configuration). A change in the circular polarization component of the luminescence intensity was detected in the Faraday configuration.

Results

Representative absorption (at 298 K) and PL (at 77 K) spectra of CD CdSe nanoparticles films, with different nanoparticle diameters, are shown in Figure 1 by the solid and dashed lines, respectively. The band gap energy was estimated by best fitting the experimental curve to a conventional direct band gap semiconductor absorption function, leading to values of 2.25, 2.03, and 1.84 eV for the 4, 6, and 20 nm samples, respectively. Thus, the absorption edge is blue-shifted upon reduction of particle size. The PL spectra, shown in Figure 1, were corrected for the system response, and for ease of comparison, their intensities were normalized to a common arbitrary scale. They consist of a relatively weak band in the green region and an additional intense band in the red-near-IR region, with a full width at half-maximum (fwhm) of about 0.5 eV. The red-IR band dominates in all the samples studied. This band is centered at 1.35, 1.43, and 1.55 eV for the 20, 6, and 4 nm samples, respectively. Hence, it is clearly blue-shifted with decreasing particle size. It should be noted that all the PL spectra shown above were recorded in a water-free atmosphere; spectral measurements under normal atmospheric humidity resulted in substantial quenching of the red-IR band and enhancement of the green band. This phenomenon will be discussed in detail elsewhere. The present document concentrates on the investigation of the origin and recombination mechanism of the red-IR emission band, utilizing ODMR spectroscopy. The ODMR spectra were measured under various experimental conditions, including different excitation and emission energies, laser excitation power, microwave (mw) audio modulation frequency, and mw power.

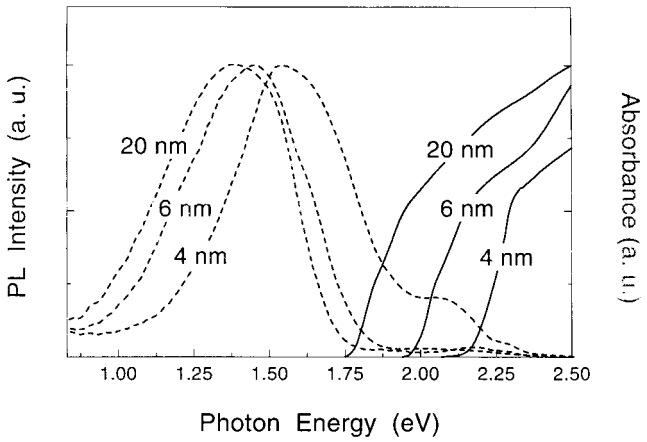

Figure 1. Absorption (solid line) and photoluminescence (dashed line) spectra of CdSe nanoparticle films with mean particle diameter as indicated in the figure.

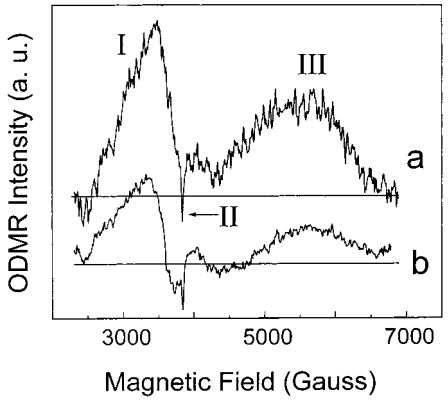

Figure 2. Representative optically detected magnetic resonance (ODMR) spectrum of CdSe nanoparticle film, recorded with laser excitation power of 6 (a) and 1.5 W/cm^2 (b).

Representative ODMR spectra of the CD CdSe nanoparticles sample, monitored at the red-IR luminescence band, are shown in Figure 2. The latter spectra were recorded at the Voight ($k_{em}\perp H_0$) configuration, with laser excitation power of 6.0 W/cm^2 (curve a) and 1.5 W/cm^2 (curve b). ODMR spectra of various CD CdSe samples, with different mean particle diameters and excited with 457.9 and 514.0 nm Ar laser lines (at a

fixed laser excitation power), were essentially the same. Nevertheless, the S/N ratio of the spectra were enhanced under the 514.0 nm excitation. Likewise, ODMR spectra recorded at the Faraday configuration (k_{em} $||H_0$) appeared to be identical to that observed under the Voight configuration. The right ($\sigma+$) and left ($\sigma-$) circular polarization components of ODMR in the latter configuration showed identical spectra.

The spectra in Figure 2 consist of three resonance signals, labeled I, II, and III. Resonance II in spectrum a is associated with quenching of the luminescence intensity (negative signals), while resonances I and III in the latter spectrum correspond to enhancement of the luminescence intensity (positive signals). Resonance II is relatively narrow with a full width at half-maximum (fwhm) of 20 G and a *g* factor of 2.00, while resonances I and III are rather broad (fwhm $\approx$ 750 G), with a *g* factor around 2.32 and 1.40, respectively. Spectrum b in Figure 2 shows reduction of the intensity of resonances I and III upon reduction of the laser power. Resonance I is accompanied by a negative tail in its high magnetic field regime.

The ODMR dependence on the mw audio modulation (AM) frequency was measured in the 100 Hz−13.0 kHz frequency range. The envelope of the ODMR spectra showed independent behavior; however, the S/N ratio varied slightly with variation of the AM frequency. This improved by a factor of 6 upon increasing the frequency from 100 Hz to 1.5 kHz, with no further variation upon increase of the frequency up to 6.5 kHz. At frequencies higher than 6.5 kHz, there was a substantial reduction in intensity of the entire ODMR spectrum. Consequently, the spectra represented in this paper were recorded with an AM frequency of 1.5 kHz. The ODMR spectra were measured in a mw power of 5−100 mW. The intensity of the entire ODMR spectrum decreased gradually with a decrease of the mw power.

Utilization of a band-pass optical filter showed that the ODMR phenomenon, in the present case, is associated solely with the red-IR emission, while the weak green band did not contribute to the magnetic resonance events. Moreover, the resonance signals recorded under various experimental conditions were independent of the orientation of the CD films and the direction of the external magnetic field, as expected from the randomly oriented nanocrystalline film.

Discussion

CdSe nanoparticles, grown by the CD method, show high crystallinity with bulk cubic crystallographic structure. Consequently, the blue shift of the absorption curve and the dominant emission band are associated with a quantum size effect. The 4 and 6 nm samples consist of nanoparticles with average diameters smaller than that of the bulk exciton (ca. 12 nm).[24] Thus, the absorption blue shift of the studied samples with respect to the bulk (with room temperature band gap of 1.84 eV) is due to a strong confinement effect. Conversely, the average nanoparticle diameter of the 20 nm sample is substantially larger than that of the bulk exciton, showing only residual confinement effects. The absence of clear exciton features in the absorption spectra may be due to the existence of the 15% size distribution and additional weak broadening due to interparticle interactions within the films.[1,21]

The PL spectra of the various samples are dominated by a red-IR emission band. Comparison between the absorption and these emission spectra (Figure 1) indicates that the maximum of the PL band is located about 0.5 eV below the corresponding absorption edge. Moreover, similar widths, shapes, and Stokes shifts of the PL band in the various samples imply that the

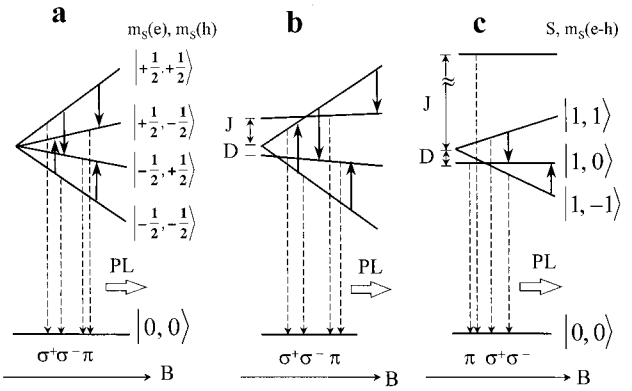

Figure 3. Spin energy level diagrams of the following cases: (a) in the absence of exchange interaction; (b) with intermediate exchange interaction; (c) with strong exchange interaction. The notations of the quantum numbers, the optical transitions, and the magnetic interactions are explained in the text.

recombination mechanism is essentially the same for the strongly and weakly confined cases. The interpretation of the PL spectra has recently been published.[21] This analysis reveals that the red-IR emission band is associated with an electron (e) and hole (h) pair recombination, trapped at imperfection sites, with an ensemble average of mutual distances. The large Stokes shift indicates that at least one trapping site is relatively deep. However, deep states are only slightly affected by the confinement process (due to the localization of their electronic wave function), and thus, the existence of quantum size effect and low effective mass of the electron ($m_e/m_h = 0.13/0.4$[24]) suggest the occurrence of a recombination between shallow trapped electrons and deep trapped holes. However, these latest results still raise several questions regarding the mechanism of recombination and the chemical nature of the trapping sites. The following paragraphs show our attempts to answer these questions via analysis of the ODMR measurements.

The ODMR spectra, discussed in the previous section, consist of three dominant resonance signals, labeled I, II, and III. Resonance II is relatively narrow and always shows a negative signal, while resonance I and III are substantially wider, with variation of the signal sign and intensity under certain experimental conditions. These differences reveal that the spin relaxation of resonance II differs substantially from that of resonances I and III. The indicated observations suggest that resonance II is associated with a singular magnetic resonance event, while resonances I and III are both correlated with another event. The origin of resonances I and III will be discussed first.

The envelope of an ODMR spectrum of trapped electrons and holes in the nanoparticle films depends on the mutual interactions between the carriers. This interaction can be explained according to the diagrams shown in Figure 3. Diagram a considers a case in which the electron and hole are spaced apart, each with a spin quantum number $S = {}^1/_2$. In this case, the e−h pair does not exhibit an exchange interaction (J), leading to a 4-fold excited spin manifold, associated with the electron [m_S(e) $= \pm{}^1/_2$] and hole [m_S(h) $= \pm{}^1/_2$] spin projections on the external magnetic field direction. The spin resonance transitions, in the latter manifold, are shown by the small arrows, while the optical transitions are given by the dashed lines. $\sigma+$ and $\sigma-$ correspond to the circular polarized transitions, while π corresponds to the unpolarized optical transitions. The corresponding ODMR spectrum should consist of two resonance signals (each doubly degenerate), associated with flipping of the electron and hole projection direction individually, and those signals may have independent behavior

when recorded under different experimental conditions. Diagram c corresponds to a case in which the e−h isotropic exchange interaction (J) is extremely large, and thus the spin manifold collapses into a singlet ($S = 0$) and triplet ($S = 1$) spin state. The $S = 1$ manifold consists of combined e−h spin projections with quantum numbers of m_S(e−h) = 1, 0, −1. In this case, the resonance transitions are associated with flipping of the e−h combined projections, as labeled by the small arrows in the diagram. Moreover, the triplet manifold may exhibit asymmetric behavior, due to the existence of a direct spin−spin interaction even in the absence of an external magnetic field. The latter is labeled D in the figure and named the zero-field splitting. Then the anticipated ODMR should consist of a resonance doublet, separated by 2D, when its components are highly correlated and change simultaneously with any change in the experimental conditions. Clearly, the spin manifold at the excited state can range from extremely weak to strong exchange interactions. For example, diagram b represents an intermediate case, in which the exchange interaction is comparable with the Zeeman splitting energy. Although the spin selection rule prohibits the magnetic transition between the singlet and triplet manifold, the existence of exchange interaction causes mixing of these spin states and consequently gives rise to some spin singlet−triplet transitions. The intermediate case shown in diagram b may also exhibit level crossing (shown in the diagram), leading to a negative signal at a particular external magnetic field.

Obviously, the similar behavior of resonance signals I and III (shown in Figure 2), under different experimental conditions, suggests that they are associated with interacting e−h pairs. Moreover, the observation of unpolarized ODMR spectra, recorded under the Voight and Faraday configuration, suggests that the spin manifold is composed of the m_e, $m_h = \pm 1/2$ projections as shown in the above figure, and excluded the existence of spins with m_e, $m_h \geq \pm 3/2$. The resonance signals can be simulated by the utilization of the following spin Hamiltonian:

$$H_s = \beta \mathbf{S}_e g_e \mathbf{H_0} + \beta \mathbf{S}_h g_h \mathbf{H_0} + \mathbf{S}_e D \mathbf{S}_h + J \mathbf{S}_e \mathbf{S}_h \qquad (1)$$

where the first two terms correspond to the effective Zeeman interaction of an electron and hole, the third term corresponds to the zero-field splitting, and the last term corresponds to an isotropic exchange interaction. It should be noted that the hyperfine interaction has been neglected in the present case; this unresolved interaction may insert some broadening to the line shape. It was assumed that the effect of anisotropy is mainly pronounced in the direct dipole−dipole and Zeeman interactions, and thus, the anisotropy in the exchange interaction has been neglected. Because of the random orientation of the nanoparticles within the film, a powder pattern spectrum had been considered. Utilization of the above Hamiltonian led to a best fitted envelope of signals I and III, as shown by the solid line in Figure 4a. The spin Hamiltonian parameters, utilized for the best fitted spectrum, are listed in Table 1. The simulation showed the necessity to include an anisotropic **g** tensor for best fitting the line shape of resonances I and III. For simplicity, the **g** tensor was assumed to be diagonal, with axial symmetry ($g_{xx} = g_{yy} \neq g_{zz}$), g_{zz} was assumed normal to the surface of the nanoparticle and $g_{xx} = g_{yy}$ tangential to it (vide infra). The standard deviations for the g and D values, indicated in the table, represent the uncertainty in the simulation. It was essential to comprise a Gaussian distribution of J values; thus, the indicated standard deviations for the J value correspond to the full-width at half-maximum of the Gaussian. The Gaussian broadening of J values includes its uncertainty and that both cannot be separated. The excited-state spin manifold, associated with resonance I and III and derived by the spin Hamiltonian calculations, is shown in Figure 5a. It exhibits an intermediate exchange interaction, with $J \neq 0$ and $D \neq 0$ and with J smaller than the Zeeman splitting energy (see Figure 3b). The theoretical spectrum associated with a single J value consists of four

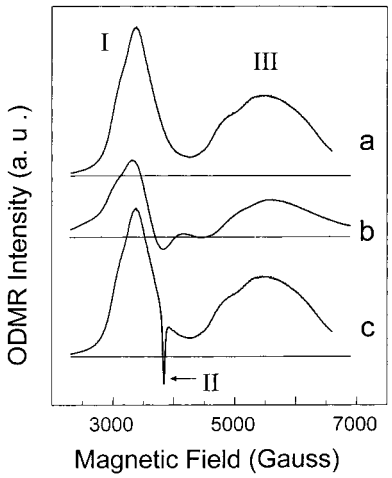

Figure 4. Simulated ODMR spectra. Curves a and b include the contribution of resonance signals I and III for laser excitation power of 6 and 1.5 W/cm^2, respectively. Curve c includes the contribution of resonance signals I, II, and III at laser excitation power of 6 W/cm^2.

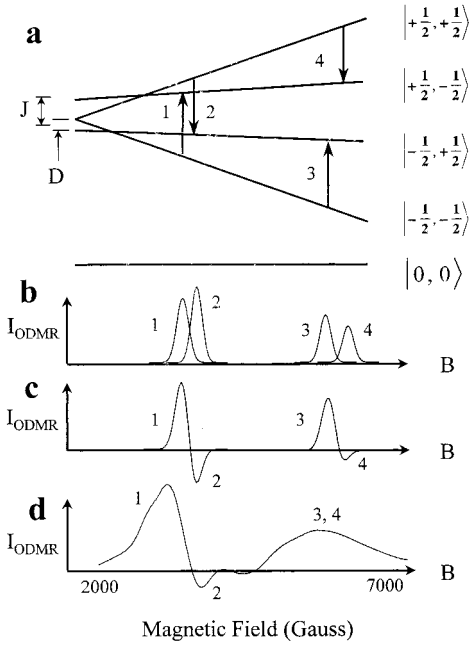

Figure 5. Spin energy level diagram, best fitting the physical phenomena in the CdSe nanoparticles, as derived from the solution of the spin Hamiltonian (eq 1): (a) anticipated spectrum for a single J value, with isotropic g factors of the recombining sites, for an unthermalized case; (b) anticipated spectrum, under the same conditions as (a), for a thermalized case; (c) anticipated spectrum for an ensemble of J values, with anisotropic g factor, for a thermalized case.

TABLE 1: Spin Hamiltonian Parameters of the ODMR Resonance Signals I, II, and III

	g_{zz}	$g_{xx} = g_{yy}$	J (meV)	D (meV)
I	1.68 ± 0.12	1.23 ± 0.12	0.0022 ± 0.0005	0.0013 ± 0.0001
II	2.000 ± 0.001	2.000 ± 0.001		
III	2.65 ± 0.08	2.30 ± 0.08	0.0022 ± 0.0005	0.0013 ± 0.0001

resonance transitions as shown in Figure 5b. Each pair of transitions is associated with flipping of the electron- or hole-spin projection. It should be noted that the appearance of $J \neq 0$ causes the transition probability into the $|+1/2, -1/2\rangle$ spin state to be slightly smaller than into the $|-1/2, +1/2\rangle$ state, thus leading to weaker intensity of the 1 and 4 signals, pronounced in the anticipated spectrum in Figure 5b. Occasionally, a distribution of J values exists, due to the existence of an ensemble of e−h pair distances. The latter causes broadening of the resonance signals and blurring of the four distinct transitions and instead causes the appearance of two envelopes. The last effect coincides with the physical phenomenon occurring in the experimental spectrum shown in Figure 2a and presented by resonance signals I and III.

The appearance of a negative tail in resonance I (Figure 2b) below a particular laser excitation power is associated with a Boltzmann distribution of carriers among the spin states. When the e−h recombination time (τ) is much faster than the spin−lattice relaxation time (T_1), i.e., $\tau \ll T_1$, then thermalization among the spin levels is avoided, leading to an unthermalized spectrum as shown in Figure 5b. However, when the recombination process occurs on a time scale more or less equivalent to the spin−lattice relaxation, $\tau \simeq T_1$, thermalization will occur. This leads to the appearance of positive and negative resonance components, as shown in parts c and d of Figure 5 for a single J and distribution of J values, respectively. It should be noted that the highest field resonance transition is substantially weaker in the thermalized case, due to the low Boltzmann population at the relevant spin states. Moreover, this high field resonance signal is blurred completely in the case where a distribution of J values exists, as evidently seen in Figure 5d. Comparison of the anticipated spectrum in Figure 5d and the simulated spectrum in Figure 4b emphasizes the necessity in considering thermalization effects and a Gaussian distribution of J values. The latter is associated with the existence of an ensemble average of e−h distances ($r_1 ... r_i$), consequently creating a distribution of e−h recombination times (τ). Thus, under relatively high excitation power (>1.5 W/cm^2), the ODMR method detects mainly the nearest e−h pairs with $\tau \ll T_1$. However, when the sample is excited with a relatively weak laser power (<1.5 mW/cm^2), then the ODMR measurements detect the trapped e−h pairs of varying distances with both $\tau \ll T_1$ and $\tau \simeq T_1$. Thus, the spectrum recorded at 6.0 W/cm^2 in Figure 2a exhibits only positive ODMR signals and is typical of an unthermalized case, while spectrum b shows positive signals and a negative tail, typical of an overlap of both thermalized and unthermalized cases.[25]

The anisotropy of the trapping sites excludes the possibility of their location at the core of nanoparticles with cubic structure and, instead, suggests their localization at the surface. (Recently, it was proposed that local defect sites do not exist at the core of nanoparticles.[15,16]) Accordingly, the distribution of exchange interaction values can be due to the existence of an ensemble of e−h pair distances, most probably around the periphery of a nanoparticle. Actually, the isotropic exchange interaction value depends on the e−h distance, and thus a distribution of this value is limited by the size of the nanoparticles. The e−h exchange interaction of the CdSe bulk exciton is 0.13 meV.[26] Efros predicted an exchange interaction of an exciton in ca. 3 nm CdSe nanocrystals of about 320 meV.[7] Thus, an exchange interaction of about $J = 0.0013$ meV is a reasonable value for separate trapped e−h pairs confined on the surface of the particle. The g values of the trapped carriers are substantially different from those of the band edge carriers ($g_e = 0.78$, $g_h = -0.96$[7]), further supporting the localization of the trapped carriers at imperfection sites with distinct electronic properties.

Several suggestions regarding the chemical nature of the trapping sites can be raised. Previous studies[19,20] suggested that deep states, in particles with nanometer dimensions, are mainly associated with surface defects. They can be associated with Cd^{2+} and S^{2-} vacancies (stoichiometric defects), dangling bonds, or external adatoms (like oxygen). It should be noted that the random orientation of the particles within the matrix prevented identification of any local crystallographic axis of the trapping sites.

The discussion so far has concentrated on the interpretation of the I and III resonance signals in the ODMR spectra. The following paragraph will give an insight into the nature of resonance II. At first glance, resonance II seems to be associated with level crossing within resonance I and III spin systems (see Figure 3b). However, this possibility is excluded due to the dissimilarity of resonance II to the other ones. Spin Hamiltonian simulation of this resonance is given by the sharp negative signal in Figure 4c (overlapping the envelopes of resonances I and III), according to the parameters given in Table 1. They are associated with a carrier, located at a highly symmetric center with $g = 2.00$, and absence of exchange or crystal field interaction. The latter behavior resembles a paramagnetic free carrier. The confinement properties of the nanoparticles may exclude the existence of such a carrier. However, if it does exist, it should be in a symmetric substitutional or interstitial position. We note that magnetic susceptibility measurements[27] of the CD CdSe nanoparticles films suggested the existence of adsorbed paramagnetic oxygen. The latter may lead to the existence of free carriers within the core or at the surface of the nanoparticle. In any event, the negative sign of the entire resonance signal II, recorded at any excitation power, corresponds to the existence of a competitive nonradiative e−h recombination process that causes quenching of the red-IR luminescence band.

Summary

The PL spectra of CD CdSe nanoparticle films are dominated by a red-IR emission band associated with the recombination of shallow trapped electrons and deep trapped holes. Theoretical simulation suggests a distribution of an exchange interaction parameter associated with the existence of a distribution of e−h pair distances. This distribution is limited by the size of the nanoparticles. The trapping sites possess low symmetry, implying their location at the nanoparticle surface. The g values of the trapped carriers differ from those of the band edge carriers, further supporting the localization of the trapped carriers at imperfection sites, with an electronic nature different from that of the band edge.

Acknowledgment. This research was supported by the Israel Ministry of Science Contract 5839-2-96 and the United States−Israel Binational Science foundation (BSF), Jerusalem, Israel, Grant 94-00103.

References and Notes

(1) Murray, C. B.; Norris, D. J.; Bawendi, M. G. *J. Am. Chem. Soc.* **1993**, *115*, 8706.
(2) Henglein, A. *Chem. Rev.* **1989**, *89*, 1861.
(3) Brus, L. E. *J. Phys. Chem.* **1986**, *90*, 2555.
(4) Ekimov, A. *J. Lumin.* **1996**, *70*, 1 and references within.
(5) Wang, Y.; Suna, A.; McHugh, J.; Hiliniski, E. F.; Lucas, P. A.; Johnson, R. D. *J. Chem. Phys.* **1990**, *92*, 6027.
(6) Wang, Y.; Herron, N. *J. Phys. Chem.* **1987**, *91*, 257.

(7) Nirmal, M.; Norris, D. J.; Kuno, M.; Bawendi, M. G.; Efros, Al. L.; Rosen, M. *Phys. Rev. Lett.* **1995**, *75*, 3728.
(8) Alivisatos, A. P. *J. Phys. Chem.* **1996**, *100*, 13226.
(9) Chopra, K. L.; Kainthla, R. C.; Pandya, D. K.; Thakoor, A. P. *Physics of Thin Films*; Acdemic Press: New York, 1982; Vol. 12.
(10) Chu, T. L.; Chu, S. S.; Ferecides, C.; Wu, C. Q.; Britt, J.; Wang, C. *J. Appl. Phys.* **1991**, *70*, 7608.
(11) Lincot, D.; Ortega-Borges, R.; Vedel, J.; Ruckh, M.; Dessler, J.; Velthaus, K. O.; Hariskos, D.; Schock, H. W. In *Proceedings of the 11th European Photovoltaic Solar Energy Conference*, Montruex, 1992; p 870.
(12) Gorer, S.; Hodes, G. *J. Phys. Chem.* **1994**, *98*, 5338.
(13) Gorer, S.; Albu-Yaron, A.; Hodes, G. *J. Phys. Chem.* **1995**, *99*, 16442.
(14) Gorer, S.; Albu-Yaron, A.; Hodes, G. *Chem. Mater.* **1995**, *7*, 1243.
(15) Tober, H.; Herhold, A. B.; Johnson, C. S.; Alivisatos, A. P. *Phys. Rev. Lett.* **1994**, *73*, 3266.
(16) Schroeder, J.; Persons, P. D. *J. Lumin.* **1996**, *70*, 69.
(17) Murray, C. B.; Norris, D. J.; Bawendi, M. G. *J. Am. Chem. Soc.* **1993**, *115*, 8706.
(18) Godstien, A. N.; Echer, C. M.; Alivisatos, A. P. *Science* **1992**, *256*, 1425.
(19) Dag, I.; Lifshitz, E. *J. Phys. Chem.* **1996**, *100*, 8962.
(20) Lifshitz, E.; Bykov, L.; Yassen, M.; Chen-Esterlit, Z. *Chem. Phys. Lett.* **1997**, *273*, 381.
(21) Lifshitz, E.; Dag, I.; Litvin, I.; Hodes, S.; Gorer, G.; Reisfeld, R.; Zelner, M.; Minti, H. *Chem. Phys. Lett.* **1998**, *288*, 188.
(22) Gorer, S.; Hodes, G. In *Semiconductor Nanoclusters*; Kamat, P. V., Meisel, D., Eds.; Elsevier Science: Amsterdam, 1996; p 297.
(23) Gorer, S.; Hodes, G. *J. Phys. Chem.* **1994**, *98*, 5338.
(24) Segall, B.; Marple, D. T. F. *Physics and Chemistry of II−VI Compounds*; Aven, M., Prener, J. S., Eds.; North-Holland: Amsterdam, 1967; p 316.
(25) Davies, J. J.; Nicholls, J. E. *J. Phys. C: Solid State Phys.* **1982**, *15*, 5321.
(26) Kochereshko, V. P.; Mikhailov, G. V.; Ural'tsev, I. N. *Sov. Phys. Solid State* **1983**, *25*, 439.
(27) Gorer, S.; Hodes, G.; Reich, S., unpublished results.